Enhancement of the Thermal Stability and Thermoelectric Properties of $Yb_{14}MnSb_{11}$ by Ce Substitution

Kasey P. Devlin[1], Jason H. Grebenkemper[1], Kathleen Lee[2], Giacomo Cerretti[2], Sabah K. Bux[2] and Susan M. Kauzlarich[1]*

[1]*Department of Chemistry, One Shields Ave, University of California, Davis, CA 95616 USA*

[2]*Thermal Energy Conversion Technologies Group, Jet Propulsion Laboratory, California Institute of Technology, 4800 Oak Grove Drive, MS 277-207, Pasadena, CA 91109*

Abstract

$Yb_{14}MnSb_{11}$ is a p-type high temperature thermoelectric material with operational temperatures as high as 1273 K. Rare earth substitution into this phase has been shown to increase the melting point further while also decreasing the sublimation rate. Solid solutions of 3+ rare earth elements with Yb^{2+} in $Yb_{14}MnSb_{11}$ have been shown to have increased stability against oxidation. Ce is an abundant rare earth element and the substitution of Ce^{3+} on the Yb^{2+} sites should increase the thermoelectric efficiency of the material due to a decrease in carrier concentration. Samples of $Yb_{14-x}Ce_xMnSb_{11}$ (x ~ 0.4) were synthesized using ball milling followed by annealing and consolidation via spark plasma sintering (SPS). The systematic addition of a small increasing excess of Mn and the resulting compositions were investigated. Small amounts of impurities in the samples, such as Yb_2O_3 and Mn, are correlated with negative attributes in the resistivity data. Hall effect measurements revealed reduced carrier concentration of ~44% at 600 K over $Yb_{14}MnSb_{11}$ and adjusting the stoichiometry towards $Yb_{13.6}Ce_{0.4}MnSb_{11}$ leads to increases in resistivity and Seebeck coefficient with a reduction in thermal conductivity. $Yb_{13.6}Ce_{0.4}MnSb_{11}$ shows an improved average ZT_{avg} = 0.80 when compared to $Yb_{14}MnSb_{11}$ (0.71) and no degradation when exposed to ambient air for 77 days at room temperature. Thermogravimetric analysis of air oxidation shows that $Yb_{13.6}Ce_{0.4}MnSb_{11}$ and $Yb_{14}MnSb_{11}$ do not oxidize until 700 K.

Introduction

Zintl phases are of interest for thermoelectric applications due to their structural complexity, leading to low thermal conductivity, and flexibility, allowing for property

tuning.[1–4] Thermoelectric materials are categorized by their dimensionless figure of merit, $zT = S^2T/\kappa\rho$, where S is the Seebeck coefficient, κ is thermal conductivity, ρ is electrical resistivity, and T is the measurement temperature. Larger zT values correlate with a more efficient material. Presently, the zT of n-type thermoelectric materials surpass p-type materials, in particular, at the highest temperatures.[5] In order for an efficient high-temperature power generating device to be transformative, the zT of p-type thermoelectric materials must be improved. Materials that show promise for long-term operation and power generation at elevated temperatures have been incorporated into NASA's efforts to advance thermoelectric energy conversion technology.[6,7] Currently, $Yb_{14}MnSb_{11}$ is one of the leading p-type thermoelectric material for high temperature applications with high thermoelectric efficiency (zT) and good stability at elevated temperatures.[8–10] $Yb_{14}MnSb_{11}$, and other high temperature materials, utilize a wide operation temperature range which allows for a larger temperature gradient between the hot and cold sides of a thermoelectric generator which allows for higher Carnot efficiencies. The relationship between Carnot efficiency and zT is illustrated by the equation $\eta_{CPM} = \frac{\Delta T}{T_h} \frac{\sqrt{1+ZT_{avg}}-1}{\sqrt{1+ZT_{avg}}+{}^{T_c}/_{T_h}}$, where η_{CPM} is the efficiency of the material based on the constant property model as described by Kim et al. and ZT_{avg} is the average ZT obtained by integration over the operational temperature range.[11,12] Therefore, new compositions of this structure type with better ZT_{avg} and high stability could provide for longer lifetimes of a radioisotope thermoelectric generator, providing space missions with higher scientific payloads for a given power level.[13]

$Yb_{14}MnSb_{11}$ crystallizes in the tetragonal $Ca_{14}AlSb_{11}$ structure, with one formula unit being described by 14 Yb^{2+} cations, a $MnSb_4^{9-}$ tetrahedron, a Sb_3^{7-} linear unit, and 4 Sb^{3-} anions,[14,15] shown in Figure 1. Yb is considered to be Yb^{2+} in this compound, confirmed by XMCD studies.[16] The high zT properties were first discovered for dense pellets prepared from single crystals.[10] A metallurgical synthesis has been developed, employing a small excess of Mn from a MnSb precursor that allows for better homogenization of the pre-reacted powders and reduction of a common impurity phase, $Yb_{11}Sb_{10}$.[8]

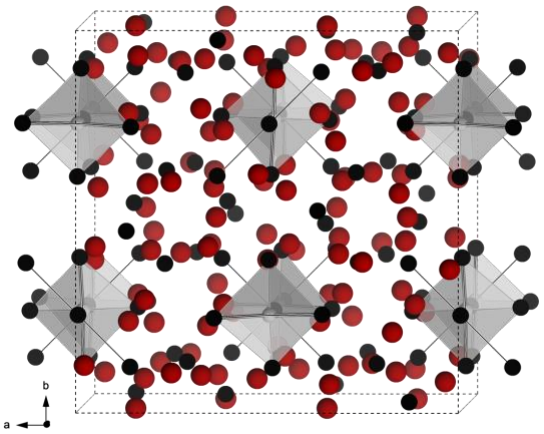

Figure 1: $Yb_{14}MnSb_{11}$ viewed down the *c*-axis (space group = $I4_1/acd$) where Yb atoms are red, $MnSb_4^{9-}$ units are grey polyhedra, and Sb atoms are black.

Many recent studies have focused on improving the thermoelectric properties of $Yb_{14}MnSb_{11}$ via substitutions. These substitutions largely target a reduction in carrier concentration, with a particular interest in the rare earth (RE) elements which are typically RE^{3+} cations and can substitute for Yb^{2+}.[17–21] The impact of La^{3+} substitution in $Yb_{14}MnSb_{11}$ on thermoelectric properties has been studied for samples prepared via Sn-flux growth.[19] The thermal conductivity of the $Yb_{13.6}La_{0.4}MnSb_{11}$ sample is decreased compared to the parent $Yb_{14}MnSb_{11}$. The Seebeck coefficient is improved to > 200 μV/K at ~ 1150 K similar to the Sc, Pr, and Tm containing compounds.[17,18,20] The resistivity is increased compared to the parent $Yb_{14}MnSb_{11}$ compound and is 9% higher at the highest temperatures compared to the Pr containing compound, which is the RE containing compound with the highest resistivity.[17–21] The resulting properties lead to a maximum *zT* of 1.15 at 1150 K, but does not exceed the best *zT* reported for $Yb_{14}MnSb_{11}$ due to bipolar conduction at the highest temperatures.[19] The oxidation kinetics of these $Yb_{14-x}RE_xMnSb_{11}$, excluding Ce and Eu, were studied. Decreased vapor pressures and increased resistance to oxidation were observed and were attributed to the formation of a protective $Yb_{2-x}RE_xO_3$ layer.[22] An increased *zT*, greater oxidation stability, and reduced vapor pressure would all be beneficial advancements for thermoelectric device design. RE^{3+} alloying has been studied in $Ca_{14}MnSb_{11}$ focusing on structure and magnetic properties, but due to sensitivity to oxidation, bulk property measurements have not yet been reported.[23]

Previous work on Ce substitution in $Yb_{14}MnSb_{11}$ has been on single crystal growth of $Yb_{14-x}Ce_xMnSb_{11}$ (x = 0 – 0.58) and focused on structure and magnetic properties.[24] Ce was found to substitute on two of the four Yb crystallographic sites (Yb(2) and Yb(4)), leading to an expansion of the unit cell and a maximum Ce incorporation of x = ~ 0.6. Magnetic susceptibility gave rise to a magnetic moment consistent with Ce^{3+}. It was found that Ce substitution led to a reduced magnetic ordering temperature, until x = 0.45, attributed to decreased carrier concentration. The ferromagnetic ordering is attributed to a RKKY mechanism, with an overall higher magnetic moment compared with $Yb_{14}MnSb_{11}$ arising from the local f^1 moment on Ce.[24]

In this paper, the effects of Ce^{3+} substitution, and the resulting reduction in carrier concentration, on the thermoelectric and thermochemical properties of $Yb_{14}MnSb_{11}$ are presented, focusing on the composition $Yb_{13.6}Ce_{0.4}MnSb_{11}$. The composition of x = 0.4 for $Yb_{14-x}Ce_xMnSb_{11}$ was chosen based on the reported optimized performance of the other light RE alloyed samples previously described.[17,18] MnSb was employed as the sources of Mn and the effect of a slight excess (up to 10%) in Mn was systematically investigated. The figure of merit is calculated and ZT_{avg} over the temperature range 475 – 1275 K is compared to $Yb_{14}MnSb_{11}$. Ambient oxidation stability of the Ce phase is investigated and compared to $Yb_{14}MnSb_{11}$. Oxidation as a function of temperature was measured via thermogravimetric analysis.

Experimental

Reagents. Dendritic Yb (99.99%, Metal Rare Earth Limited), Ce rod (99.9% Alfa Aesar), La rod (Ames Lab), Mn pieces (99.95%, Alfa Aesar), and Sb shot (99.999%, Alfa Aesar) were used for the following synthesis. All elements were handled in an argon-filled drybox with moisture levels <1 ppm. Yb was brushed to remove any surface oxide and filed using a hardened steel rasp. Similarly, Ce was brushed to remove any surface oxide and was cut into pieces approximately the size of the filed Yb. MnSb was prepared by melting the elements together in a 1:1 ratio in a BN crucible sealed in a fused silica ampoule at 850˚C for 48 h and cooled to room temperature. The products of the MnSb synthesis are shown in Supporting Information (SI), Figure S1. Due to an excess of Sb seen in the powder X-ray diffraction (PXRD) pattern, electron microprobe analysis (EPMA) was used to determine the final excess Mn amount in each sample.

Synthesis. Samples of $Yb_{13.6}Ce_{0.4}MnSb_{11}$ were prepared using an adaptation of the previously published ball milling synthesis.[8] A particular concentration of RE^{3+} was chosen, Ce = 0.4, as it represented a RE content that has been confirmed by single crystal flux synthesis and investigated for thermochemical properties in the case of RE = La.[19] Each 5-gram reaction of $Yb_{13.6}Ce_{0.4}MnSb_{11}$ was loaded into a 5 mL WC lined grinding vial with two ~4 gram WC balls. The grinding vial was sealed under argon in polybags and mechanically agitated in a SPEX 8000M mixer mill. To investigate the effect of excess Mn on the final product, all compositions were synthesized by milling for 15 minutes with variable amounts of MnSb (*y*) and 11-*y* of Sb to achieve the desired molar ratio of 11Sb according to $Yb_{13.6}Ce_{0.4}MnSb_{11}$. After 15 minutes, the Yb and Ce were added and the mixtures were agitated for 2 × 30 minute milling cycles, scraping the walls of the container in between each run. The obtained powder was welded shut under Ar in a Nb tube (7 cm), which was then sealed under vacuum in a fused silica ampoule and annealed at 1100˚C for 96 hours. Additionally, a series of samples with an excess of Mn (1.05 Mn) with various amounts of oxide, in the final product, were also prepared according to the above synthesis and properties measured.

Spark Plasma Sintering. The powdered samples were consolidated into dense (>95%) pellets using a Dr. Sinter-Lab SPS-211LX. The powders were sieved (100 mesh) and loaded into graphite dies with an inner diameter of 12.7 mm, a height of 30 mm, and a 30 mm outer diameter. A hole in the die for thermocouple placement allowed for precise control over the temperature profile during the sintering process. The samples with nominal compositions of $Yb_{13.6}Ce_{0.4}MnSb_{11}$ were compacted by applying a force of 6 kN under vacuum, and then heated to 750 ˚C over 4 minutes. Subsequently, the applied force was increased to 10 kN while the temperature was raised to 800˚C over 1 minute, and then held for 10 minutes, yielding pellets of >95% density. The samples were sliced into two halves of approximately 1.5 mm thickness and polished for thermoelectric property measurements.

Electron Microprobe (EPMA). After TE measurements, pieces of the consolidated pellets were placed in epoxy and polished, followed by analysis with a Cameca SX-100 Electron Probe Microanalyzer with five wavelength-dispersive X-ray spectrometers (WDS). Back scattered electron (BSE) images and elemental X-ray mapping were employed to understand the distribution of dopants and any impurity phases. Ten points with a spot

size of 1 μm were analyzed with quantitative analysis to determine elemental composition. The elements were standardized with an $Yb_{14}MnSb_{11}$ single crystal for Yb, Mn metal for Mn, Sb metal for Sb, and CeO_2 for Ce. The composition of each sample was determined by calculating the average and standard deviation of 10 data points of the main phase and restraining the total atoms to 26. To differentiate the samples, they will be written $Yb_{13.6}Ce_{0.4}MnSb_{11}$ (*z* Mn), where *z* is the Mn total determined from EPMA.

Powder X-ray Diffraction. Powder X-ray diffraction (PXRD) patterns were collected on ground samples after thermoelectric data collection using a Bruker D8 Advance X-ray diffractometer utilizing Cu Kα radiation in the 2θ range 20˚ - 80˚ with a step size of 0.02˚ operated at 40 KV and 25 mA. Rietveld refinements were performed on the diffraction patterns using GSAS-II[25] to determine unit cell parameters and weight percentages of any impurity phases present. Extended oxidation studies of $Yb_{14}MnSb_{11}$ and $Yb_{13.6}Ce_{0.4}MnSb_{11}$, with a 2 wt % Si standard, were performed by solvent smearing (to create adhesion) the finely ground powder onto a zero background diffraction plate and leaving the sample on the diffraction plate for the duration of the experiment. A diffraction pattern was collected at 0, 1, 7, 21, 35, and 49 days. Initially, after 35 days, the $Yb_{14}MnSb_{11}$ sample lost adhesion suggesting that the surface chemistry had changed (presumably through surface oxidation), although there were no apparent relative intensity changes in PXRD pattern prior to the adhesion loss. Another run was initiated and this time after 49 days, the $Yb_{14}MnSb_{11}$ sample lost adhesion. The data collection for $Yb_{13.6}Ce_{0.4}MnSb_{11}$ was continued for 77 days with no evidence for cracking, adhesion loss to the plate, or color change.

Thermal Conductivity. Thermal diffusivity was measured on polished discs of the consolidated pellets employing a Netzsch LFA 457 laser flash system. Thermal conductivity is obtained from the equation, $\kappa = D \times \rho \times C_P$, where *D* is the measured thermal diffusivity, ρ is the density, and C_P is the heat capacity. Temperature dependent density was determined using previously measured temperature dependent thermal expansion for $Yb_{14}MnSb_{11}$[26] and the sample densities at room temperature. Heat capacity values were adapted from previously measured values for $Yb_{14}MnSb_{11}$.[8] The experimental data, SI, Figure S2, are plotted versus temperature.

Seebeck and Resistivity Measurements. Seebeck and electrical resistivity measured at NASA's Jet Propulsion Laboratory were performed on 12.7 mm consolidated pellets from 300 K to 1273 K. The Seebeck coefficient was measured under high vacuum using a custom-fabricated apparatus that employed the light-pulse method with tungsten-niobium thermocouples.[27] Temperature dependent Hall coefficient and electrical resistivity were measured using the Van der Pauw method with a 0.8 T magnet with tungsten pressure contact probes at a heating rate of 180K/hr in a custom-fabricated instrument.[28] The experimental data, SI, Figure S2, are plotted versus temperature.

Thermogravimetry/Differential Scanning Calorimetry (TG/DSC). Data were collected on a Netzsch STA 449 F3 using the SiC furnace. After the baselines were established, small pieces of the consolidated pellet were loaded into an alumina crucible. Samples were heated from room temperature to 1273 K, under 50 mL/min dry air flow at a heating rate of 10 K/min. Additional samples were cycled from 300 K – 1573 K, under 50 mL/min argon flow at a heating rate of 10 K/min.

Results & Discussion

Samples with nominal compositions of $Yb_{13.6}Ce_{0.4}MnSb_{11}$ were prepared via milling of the elements, annealing and spark plasma sintering the powder into fully dense pellets. The composition indicated here with ~0.4 Ce represents a composition close to the maximum RE content found in the case of Sn-flux single crystal synthesis.[24] In this study, Mn metal content was provided by MnSb and a slight excess of up to 10% was investigated. MnSb provides a higher molecular weight starting material and undergoes a peritectic decomposition at 840 ˚C,[29] providing a good precursor to disperse the low amounts of Mn needed for this compound.

Composition

BSE images and elemental mapping from EMPA utilizing WDS for $Yb_{13.6}Ce_{0.4}MnSb_{11}$ samples after SPS are provided in the SI, Figure S3. Quantitative analysis of the majority phase is presented in Table 1. The Mn content was systematically increased to determine the impact on phase purity and composition. This strategy has been shown to provide optimal thermoelectric properties in the case of $Yb_{14}MnSb_{11}$.[8] The sample resulting in 1 Mn

was found to be stoichiometric for both total rare earth (Yb + Ce) and Sb and close to the desired formula of $Yb_{13.6}Ce_{0.4}MnSb_{11}$, z = 1 Mn. Samples prepared with excess Mn show a slight deficiency of the total rare earth (Yb + Ce) amount and excess Mn, presumably at the grain boundaries in the form of Mn metal. Elemental mapping of Mn shows localized spots of high concentration for the samples prepared with the highest amounts of excess Mn (SI, Figure S3). In the following discussion, *z* indicates the Mn composition from microprobe, *y* indicates the amount of Mn employed in the synthesis.

Table 1: Quantitative Analysis of the Majority Phase of $Yb_{14-x}Ce_xMnSb_{11}$ (z Mn) from EMPA

Sample	At %					Formula
	x	Yb	Ce	Mn	Sb	
$Yb_{13.6}Ce_{0.4}MnSb_{11}$ (1 Mn)	0.4	52.3(1)	1.40(2)	3.82(9)	42.5(1)	$Yb_{13.60(3)}Ce_{0.363(5)}Mn_{0.99(2)}Sb_{11.05(3)}$
$Yb_{13.6}Ce_{0.4}MnSb_{11}$ (1.05 Mn)	0.4	51.9(2)	1.48(4)	4.02(6)	42.6(2)	$Yb_{13.49(5)}Ce_{0.39(1)}Mn_{1.05(2)}Sb_{11.08(4)}$
$Yb_{13.6}Ce_{0.4}MnSb_{11}$ (1.07 Mn)	0.4	51.6(1)	1.69(8)	4.10(6)	42.57(7)	$Yb_{13.43(3)}Ce_{0.44(2)}Mn_{1.07(2)}Sb_{11.07(2)}$
$Yb_{13.6}Ce_{0.4}MnSb_{11}$ (1.1 Mn)	0.4	51.7(3)	1.55(5)	4.2(1)	42.6(3)	$Yb_{13.44(7)}Ce_{0.40(1)}Mn_{1.09(3)}Sb_{11.07(7)}$

Rietveld refinement of a representative PXRD pattern for $Yb_{13.6}Ce_{0.4}MnSb_{11}$ is shown in Figure 2. In addition to the $Yb_{13.6}Ce_{0.4}MnSb_{11}$ phase, a small amount of Yb_2O_3 is present; likely in the form of $Yb_{2-x}Ce_xO_3$ due to an increase in the lattice parameters of the oxide component in the refinement, consistent with the CeO_2 – Yb_2O_3 phase diagram.[30,31] A summary of the unit cell and Rietveld refinement parameters for the $Yb_{13.6}Ce_{0.4}MnSb_{11}$ (*z* Mn) samples are presented in Table 2 and the refined PXRD patterns are provided in SI, Figures S4 – S6. The unit cells are consistent with the nominal composition of Ce ~ 0.4 with differences in the unit cell volume between samples being less than 1%. As the Ce content slightly increases from 0.363(5) to 0.44(2), the volume also systematically increases. For the 1.1 Mn sample, the Ce content is approximately the same as the 1.05 Mn sample but the unit cell volume is smaller. Therefore, excess Mn does not contribute to a unit cell expansion (no interstitial sites) and the excess Mn is imaged as localized high concentration spots in the elemental mapping of the sample (SI, Figure S3). The unit cell volume is consistent with what has been reported for the various rare earth alloyed samples and is about the same as what has been reported for RE = La[32] and slightly larger

than RE = Pr, Sm, Sc, and Y.[17,18] Most samples have a small amount of oxide impurity (less than 3%). $Yb_{11}Sb_{10}$ is a common impurity in $Yb_{14}MnSb_{11}$ and has been discussed in detail previously.[8] All refinements were performed initially with the $Yb_{14}MnSb_{11}$ structure, then the difference plot was inspected to determine whether to add Yb_2O_3 and $Yb_{11}Sb_{10}$. If the addition of $Yb_{11}Sb_{10}$ had no positive effect on the difference plot, it was removed from the refinement. Because the impurities are small and consistent for all samples, we can assume that the systematic changes in properties are intrinsic to the composition.[33]

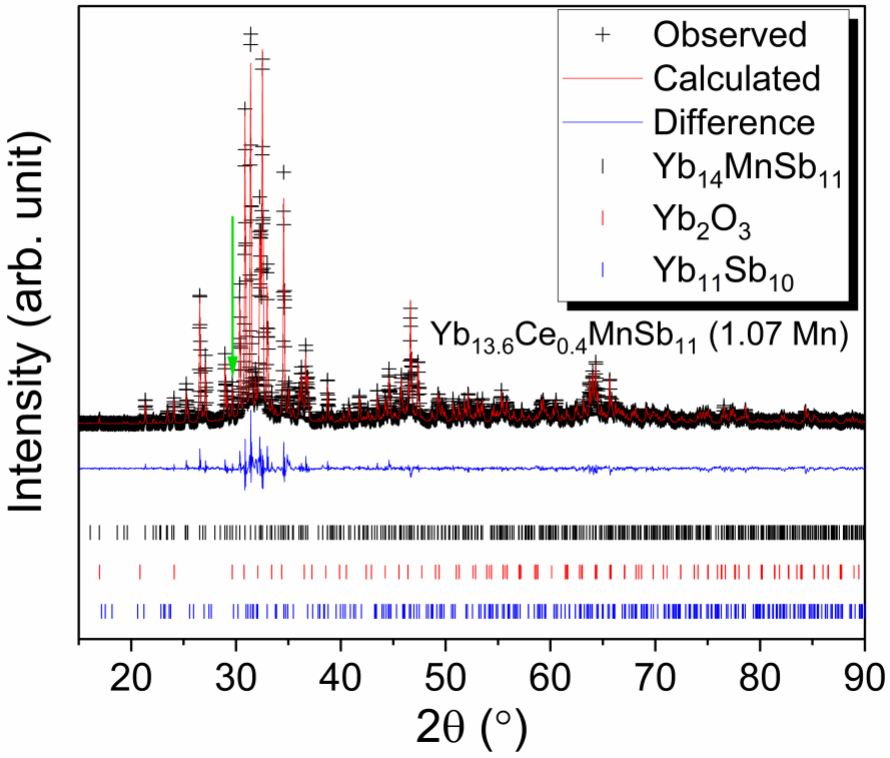

Figure 2: $Yb_{13.6}Ce_{0.4}MnSb_{11}$ (1.07 Mn)**:** Representative PXRD pattern of $Yb_{13.6}Ce_{0.4}MnSb_{11}$ where the collected data (black) is compared to the calculated pattern (red), the difference plot is illustrated in blue, and the highest intensity Yb_2O_3 peak is indicated with a green arrow.

Table 2: Unit Cell and Rietveld Refinement Parameters for $Yb_{13.6}Ce_{0.4}MnSb_{11}$ (*z* Mn) Samples from PXRD

	a (Å)	*c* (Å)	*V* (Å^3)	*Rp* (%)	*Rwp* (%)	Yb_2O_3 (Wt %)	$Yb_{11}Sb_{10}$ (Wt %)
$Yb_{13.6}Ce_{0.4}MnSb_{11}$ (1 Mn)	16.6478(1)	22.0317(2)	6106.10(9)	4.20	5.55	2.45(6)	-----
$Yb_{13.6}Ce_{0.4}MnSb_{11}$ (1.05 Mn)	16.6510(3)	22.0324(5)	6108.6(2)	7.53	9.75	2.50(9)	3.6(2)
$Yb_{13.6}Ce_{0.4}MnSb_{11}$ (1.07 Mn)	16.6421(1)	22.0084(2)	6095.42(9)	7.00	8.94	1.76(5)	2.2(1)
$Yb_{13.6}Ce_{0.4}MnSb_{11}$ (1.1 Mn)	16.6400(1)	22.0186(3)	6096.7(1)	10.41	12.85	2.72(8)	1.5(2)

Electrical Resistivity

In this study, the Ce concentration, the excess Mn, and differences in oxide percentage are considered. In previous studies,[8] samples with >10% $Yb_{11}Sb_{10}$ were studied and revealed to have no effect on the properties; therefore, since the samples in this study have <10% $Yb_{11}Sb_{10}$, there should be no impact to the transport properties. $Yb_{11}Sb_{10}$ is metallic with a resistivity below 2 mΩ-cm from 300 – 1000 K. It has an extremely small Seebeck coefficient, never surpassing 25 uV/K and a high thermal conductivity of ~12 mW/cm-K at 300 K and reaching a maximum of ~30 mW/cm-K at 1000 K.[34] If $Yb_{11}Sb_{10}$ impurities were to have an impact to the measured properties, the result would be to decrease resistivity, decrease Seebeck, and increase thermal conductivity. Since none of these changes were observed, we can state with confidence that none of the changes in thermoelectric transport is conducible to the presence of minor $Yb_{11}Sb_{10}$ impurities.

Figure 3 illustrates the temperature dependence of electrical resistivity where there are two major features: an increased room temperature resistivity and a bend-over in resistivity at high temperatures. As expected, all of the nominally $Yb_{13.6}Ce_{0.4}MnSb_{11}$ (*z* Mn) samples show an increased resistivity compared to $Yb_{14}MnSb_{11}$ (data taken from Ref.[8]). In general, the temperature dependence of the resistivity closely resembles the reported resistivities of the $Yb_{13.6}RE_{0.4}MnSb_{11}$ (RE = Y, Sc, and Pr) while the 1.05 Mn and 1.07 Mn samples more closely resemble the resistivity of RE = La and the higher RE content phase $Yb_{13.47}Sm_{0.53}MnSb_{11}$ due to the more pronounced bend-over in

resistivity.[18,19] There are two major differences between samples, that is in Ce content and excess Mn. As the Ce content increases, we expect resistivity to increase since Ce^{3+} donates an additional electron compared with Yb^{2+}. This is the case for these samples with the outlier being the one with the highest Mn loading (1.1 Mn), which contains about the same amount of Ce as the 1.05 Mn sample. The stoichiometric phase sample (1 Mn) is close in resistance to the parent $Yb_{14}MnSb_{11}$ sample at room temperature but deviates quickly as temperature increases. For samples with excess Mn, the electrical resistance at room temperature starts at a slightly higher value and then increases significantly with temperature. The temperature dependence of the resistivity of the 1.05 and 1.07 Mn samples is similar. The 1.1 Mn sample shows the largest increase in room temperature resistivity and deviation as temperature increases. There is also a bend-over in the high temperature regime that becomes more pronounced with increasing both Ce content and Mn. At the maximum loading of Mn, the bend-over is shifted to lower temperature and is more pronounced. This bend-over in resistivity at high temperatures has been previously attributed to either bipolar conduction[35–37] or to the presence of >10% $Yb_{11}Sb_{10}$[8,18] which has a melting point of ~1300 K.[34] In these samples, $Yb_{11}Sb_{10}$ is present in a very small amount, significantly less than what has been shown to cause a bend-over in $Yb_{14}MnSb_{11}$. The bend-over will be discussed further with carrier concentration.

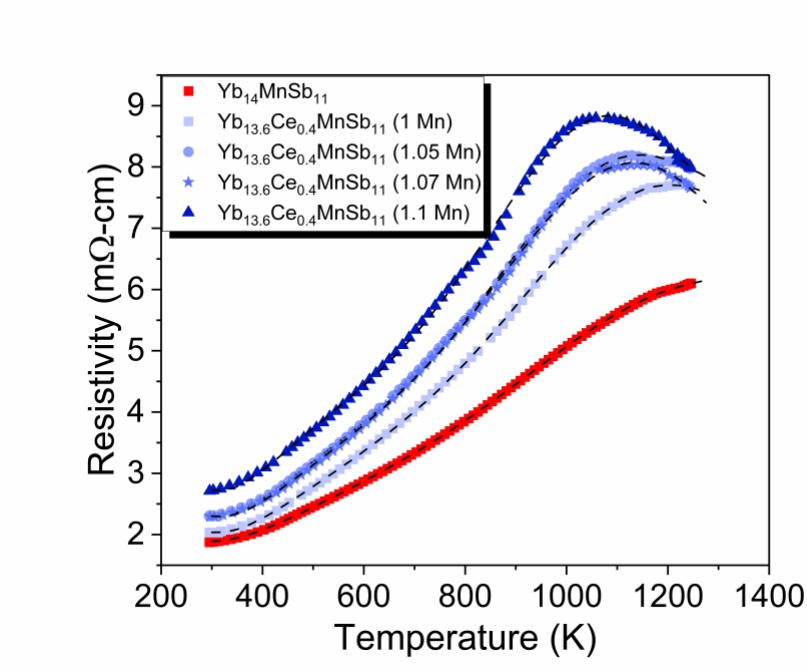

Figure 3: Electrical resistivity vs temperature of $Yb_{13.6}Ce_{0.4}MnSb_{11}$ (*z* Mn) samples compared with $Yb_{14}MnSb_{11}$ (data from Ref. [8]) where the black dashed lines are the fits used to calculate *zT*.

The resistivity results are in line with the observed carrier concentration provided in Table 3. The estimated error in the measurement is within 5%.[28] The addition of Ce decreases the carrier concentration of $Yb_{14}MnSb_{11}$, and this is more evident at higher temperatures. Compared to the other Ce containing samples, the 1 Mn sample has a slightly larger carrier concentration and contains the least amount of Ce based on EPMA compared with the two samples prepared with a slight excess (1.05 Mn, 1.07 Mn), which have similar amounts of Ce. It would be expected that the 1.1 Mn sample would also have a similar carrier concentration to the 1.05 and 1.07 Mn samples; however, it is much lower at 600 K. This is likely due to Mn at the grain boundaries contributing to the scattering of charge carriers. At high temperatures, effects from impurities at the grain boundaries are less obvious; therefore, the carrier concentrations of the 1.05, 1.07, and 1.1 Mn samples are all comparable at 1000 K.

Since Ce^{3+} contributes one additional electron, the trend in the reduction in carrier concentration is as expected. The correlation between carrier concentration and Ce incorporation is also seen in the electrical resistivity, Figure 3, where the 1 Mn sample has a slight bend-over at higher temperatures, which is less pronounced, than the 1.05 Mn and 1.07 Mn samples. Although, the 1.1 Mn sample has a similar carrier concentration and Ce incorporation, the electrical resistivity is significantly higher and bend-over is shifted to lower temperature and is more pronounced.

Table 3: Carrier Concentration at 600 and 1000 K for $Yb_{13.6}Ce_{0.4}MnSb_{11}$ (*z* Mn) Samples

	$Yb_{14}MnSb_{11}$*	$Yb_{13.6}Ce_{0.4}MnSb_{11}$ (1 Mn)	$Yb_{13.6}Ce_{0.4}MnSb_{11}$ (1.05 Mn)	$Yb_{13.6}Ce_{0.4}MnSb_{11}$ (1.07 Mn)	$Yb_{13.6}Ce_{0.4}MnSb_{11}$ (1.1 Mn)
Temperature (K)	Carrier Concentration (carriers/cm^3)‡				
600	8.06×10^{20}	5.27×10^{20}	4.51×10^{20}	4.45×10^{20}	3.91×10^{20}
1000	1.10×10^{21}	5.40×10^{20}	5.10×10^{20}	4.70×10^{20}	4.61×10^{20}

*The $Yb_{14}MnSb_{11}$ carrier concentrations are from Grebenkemper et al.[8]

‡The estimated error of the measurement is 5%.[28]

Effect of Oxide on RT Resistivity

Figure 4 compares the room temperature electrical resistivity as a function of oxide content for a series of samples prepared with the same composition (1.05 Mn). The varying amounts of oxide determined from Rietveld refinement and the relative thermoelectric properties have been compared (SI, Figure S7, Table S1). For this analysis only the room temperature resistivity is considered. As illustrated in Figure 4, as the percent oxide increases in a series of samples prepared analogously, $Yb_{13.6}Ce_{0.4}MnSb_{11}$ (y = 1.05 Mn), the RT resistivity increased linearly. This clearly shows that small amounts of oxide can have an impact on the resistivity of the samples. In previous alloying studies of the cation site, the room temperature resistivity does not increase as a function of dopant;[18–20,38] therefore, any increase in room temperature is attributed to a secondary phase. These Ce alloyed samples contain <10% $Yb_{11}Sb_{10}$; therefore, the presence of Yb_2O_3 is likely a contributing factor. Since the 1.1 Mn sample has a comparable amounts of Ce and oxide as the sample with 1.05 Mn, we attribute both the larger room temperature resistivity and the pronounced bend-over to the presence of excess Mn, possibly in the form of Mn metal at the grain boundaries. In any case, these results illustrate that a small amount of excess Mn assists in reducing the amount of $Yb_{11}Sb_{10}$ without a significant impact on electrical resistivity, but further excess results in an overall negative effect.

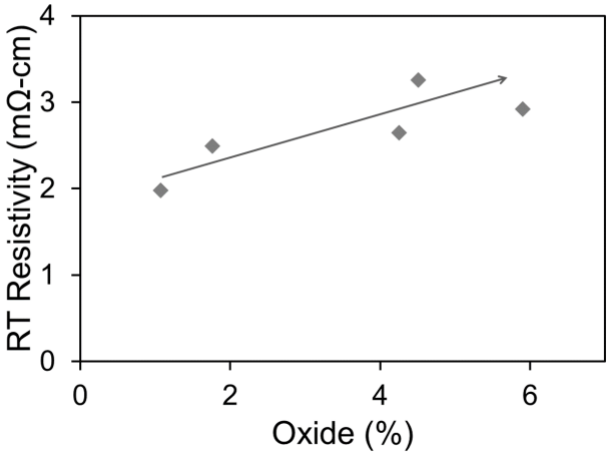

Figure 4: Yb_2O_3 content in $Yb_{13.6}Ce_{0.4}MnSb_{11}$ (y = 1.05 Mn) samples vs room temperature resistivity.

Thermal Conductivity

Figure 5 illustrates the total and lattice thermal conductivity. The thermal conductivity of $Yb_{14}MnSb_{11}$ decreases with the addition of Ce. The $Yb_{13.6}Ce_{0.4}MnSb_{11}$ (1 Mn) has a slightly higher thermal conductivity compared to the other alloyed samples. This is attributed to the lower electrical resistivity and the lower Ce content, as shown via EPMA. The other compositions have a more similar Ce content and therefore have a comparable thermal conductivity with respect to each other. The lattice thermal conductivity of the Ce containing samples is slightly lower compared to the parent $Yb_{14}MnSb_{11}$; however, the decrease above 875 K is more drastic. Similarly, other rare earth doped compositions such as Pr, Sm, Sc, and Y, show a decrease in the lattice thermal conductivity of $Yb_{14}MnSb_{11}$ by a similar magnitude as the Ce alloyed samples.[17,18]

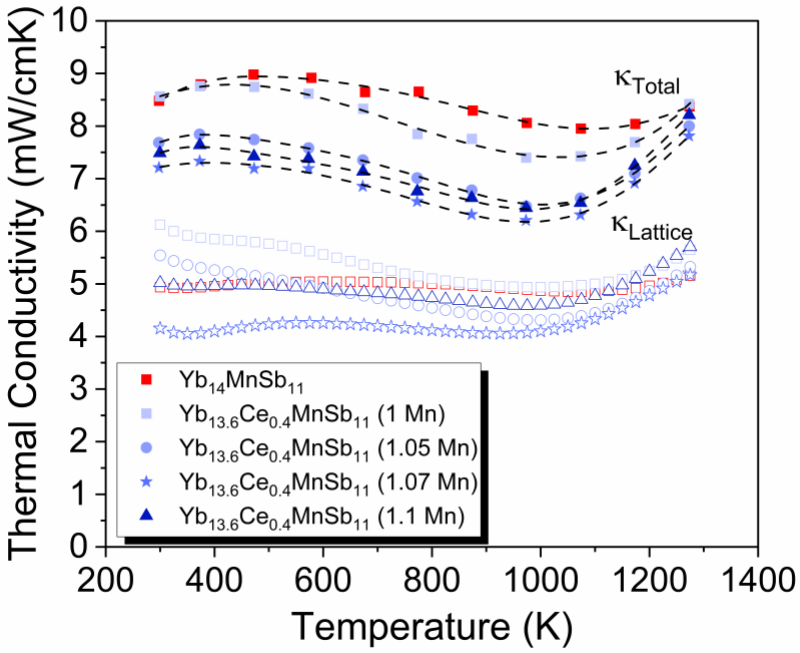

Figure 5: Thermal conductivity vs temperature of $Yb_{13.6}Ce_{0.4}MnSb_{11}$ (*z* Mn) samples compared with $Yb_{14}MnSb_{11}$ from ref [8]. Solid symbols are κ_{total}, open symbols are $\kappa_{lattice}$, color varies according to the sample compositions (*z* Mn), and the black dashed lines are the fits used to calculate *zT*.

Seebeck Coefficient

The temperature dependent Seebeck coefficient of the various $Yb_{13.6}Ce_{0.4}MnSb_{11}$ samples are shown in Figure 6. $Yb_{13.6}Ce_{0.4}MnSb_{11}$ samples have a larger Seebeck coefficient over $Yb_{14}MnSb_{11}$.[8] As the amount of Ce in the samples increase, the Seebeck coefficient increases, and this trend is in agreement with the observed increase in electrical resistivity. Additional Mn appears to have little effect until 1.1 Mn, where excess Mn may contribute to the slightly lower Seebeck values at high temperature. These Seebeck coefficients are comparable to La, Pr, and Sm substituted $Yb_{14}MnSb_{11}$, and slightly higher than Tm substituted. Similarly, there is a bend-over in Seebeck just before reaching the maximum temperature.[18,19,39] Therefore, it appears that the electrons localized in the *f* orbitals of Ce are not contributing to the Seebeck coefficients. Typically, a bend-over in the Seebeck coefficient at high temperatures is attributed to the onset of bipolar conduction and can be employed to determine a band gap using the Goldsmid-Sharp equation.[35,36] In these samples, the bend-over shifts slightly from sample to sample correlated with the slight difference in Ce concentration (Table 1); therefore, the sample with the largest Seebeck coefficient, 1.07 Mn, was used to calculate the band gap of $Yb_{13.6}Ce_{0.4}MnSb_{11}$.

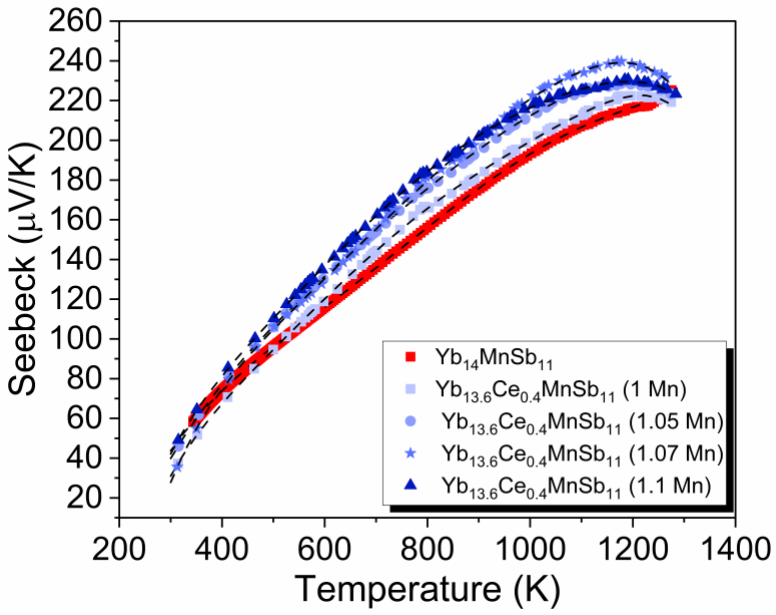

Figure 6: Seebeck coefficient vs temperature of $Yb_{13.6}Ce_{0.4}MnSb_{11}$ (*z* Mn) samples compared with $Yb_{14}MnSb_{11}$, taken from Ref. [8], where the black dashed lines are the fits used to calculate *zT*.

The smaller bandgap in $Yb_{14-x}RE_xMnSb_{11}$ compared to $Yb_{14}MnSb_{11}$ is attributed to the additional electron donated by the 3+ RE ion.[32,40] The Goldsmid-Sharp equation was originally used to calculate the band gap of ~0.5 eV for $Yb_{14}MnSb_{11}$.[10] The properties of $Yb_{14}MnSb_{11}$ have since been optimized by Grebenkemper et al.,[8] therefore, utilizing the Grebenkemper et al. data[8] at the highest measured temperature (similar to Brown et al.[10]) results in a new value of 0.57 eV. The band gap of ~ 0.6 eV is more similar to the predicted band gap from calculated electronic band theory of ~ 0.8 eV by Wang et al.[41] Calculating the band gap of $Yb_{13.6}Ce_{0.4}MnSb_{11}$ (1.07 Mn) from the bend-over in the Seebeck coefficient we find a band gap of 0.52 eV. This supports the hypothesis that the addition of the Ce^{3+} is reducing the bandgap and aiding in the activation of minority charge carriers at lower temperatures.

zT

The *zT* for each sample was calculated from fitting the above properties, Figure 7. $Yb_{14}MnSb_{11}$ (1.05 Mn) has a higher *zT* than the $Yb_{13.6}Ce_{0.4}MnSb_{11}$ at the maximum temperature due to the Seebeck bend-over in the Ce alloyed compositions. These *zT* values are comparable to the *zT* observed for La and Pr substituted $Yb_{14}MnSb_{11}$ and higher than that of Tm and Sm substituted.[18,19,39] In the case of $Yb_{14}MnSb_{11}$, it was found that a small amount of extra Mn (1.05 Mn) removes the high temperature bend-over in the Seebeck and resistivity data, presumably by removing most of the $Yb_{11}Sb_{10}$ side product. This is not the case with $Yb_{13.6}Ce_{0.4}MnSb_{11}$ due to the activation of minority charge carries; however, 1.07 Mn leads to the optimization of the properties of the Ce alloyed sample leading to an increase in *zT* below 1230 K. This sample contained the highest amount of Ce, the lowest amount of oxide, and a minor amount of $Yb_{11}Sb_{10}$ leading to an overall optimized *zT*. Additional Mn beyond the 1.07 Mn loading results in increased resistivity and a bend-over at the highest temperatures for both Seebeck and resistivity that contributes to a lower *zT*. Single crystal Ce alloyed samples showed that the maximum amount could be Ce = 0.6,[24] so it may be possible to optimize *zT* further by combining with other substitutions. Grebenkemper et al. reported similar results in optimizing the $Yb_{14}MnSb_{11}$ phase where a loaded excess of 1.05 Mn inhibited the formation of $Yb_{11}Sb_{10}$ and the sample beyond the 1.05 MnSb loading, 1.10 Mn, showed an increased resistivity with a slight bend-over, not present in the 1.05 Mn sample.[8] Additionally, the Yb_2O_3 impurity results in increased resistivity and therefore has a detrimental effect on *zT*. The

ZT_{avg}[11] calculated for the $Yb_{14}MnSb_{11}$ (1.05 Mn) and $Yb_{13.6}Ce_{0.4}MnSb_{11}$ (1.07 Mn) samples from 475 K to 1275 K are 0.71 and 0.80, respectively, amounting to a > 10% increase in ZT_{avg}. Due to the onset of the bipolar conduction, a device employing the Ce containing materials would be optimized at a maximum temperature of 1075 K. The ZT_{avg} calculated for the $Yb_{14}MnSb_{11}$ (1.05 Mn) and $Yb_{13.6}Ce_{0.4}MnSb_{11}$ (1.07 Mn) samples from 475 K to 1075 K are 0.57 and 0.68, respectively, amounting to an almost 20% increase in ZT_{avg}.

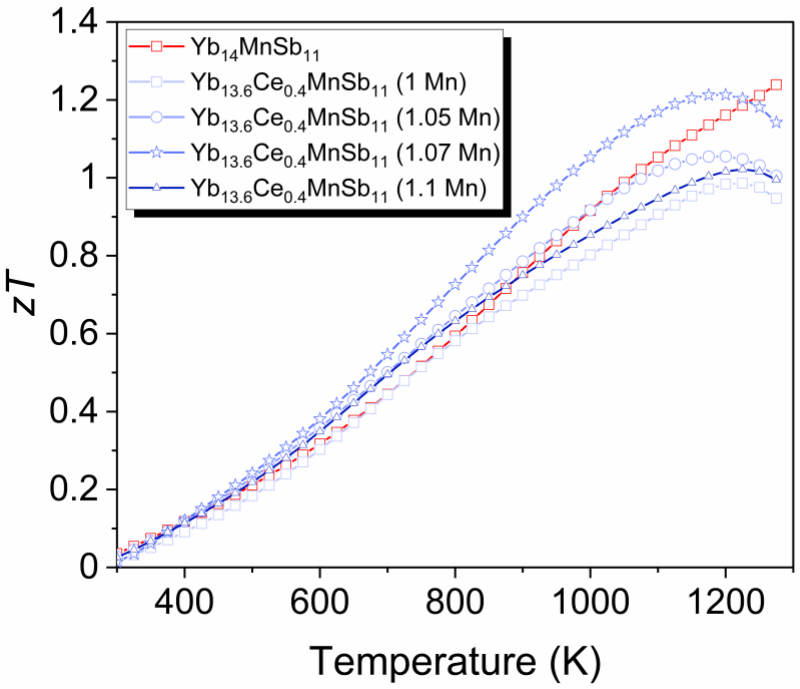

Figure 7: *zT* vs temperature of $Yb_{13.6}Ce_{0.4}MnSb_{11}$ (*z* Mn) samples compared with $Yb_{14}MnSb_{11}$, taken from ref [8].

Oxidative Stability

The oxidation of $Yb_{14-x}RE_xMnSb_{11}$ (RE = La, Pr, Nd, Sm, Gd, Tb, Dy, Ho, Er, Tm, and Lu) single crystals were studied and the crystals with $Yb_{13.56}RE_{0.44}MnSb_{11}$ (RE = La, Pr, and Nd) compositions are characterized by decreased vapor pressures and an increased resistance to oxidation attributed to self-passivation of a $Yb_{2-x}RE_xO_3$ oxide layer when compared to $Yb_{14}MnSb_{11}$.[22,42] However, a Ce containing compound was not included in the materials studied.

We expect that RE = Ce would follow the same oxidation behavior exhibited by RE = La.[22] We measured the powder diffraction pattern of a sample maintained under ambient conditions over a duration of 77 days. The sample with a stoichiometry of $Yb_{13.6}Ce_{0.4}MnSb_{11}$ (1.07 Mn) was left in air on a substrate and data were collected periodically, Figure 8. Figure 8A illustrates the highest intensity peak of the Si standard (1 1 1), while Figure 8B illustrates the highest intensity peak of the Yb_2O_3 phase (2 2 2), and Figure 8C shows the highest measured intensity (2 5 3) peak in the $Yb_{13.6}Ce_{0.4}MnSb_{11}$ diffraction pattern. Figure 8A shows that there is some experimental variation in the collected patterns. Figure 8B and C show that the $Yb_{13.6}Ce_{0.4}MnSb_{11}$ sample is stable in air, at room temperature, for at least 77 days. $Yb_{14}MnSb_{11}$ also showed little or no changes in intensity for a sample maintained under ambient conditions for 44 days. There was loss of sample adhesion to the plate after that time presumably due to surface oxidation that was not apparent by PXRD which is consistent with surface oxidation observed by XPS and XMCD, SI, Figure S8.[16,43]

Additionally, samples of $Yb_{13.6}Ce_{0.4}MnSb_{11}$ and $Yb_{14}MnSb_{11}$ were heated under flowing dry air to examine the onset temperature for oxidation, Figure 9. Both materials are resistant to oxidation until above 673 K after which the materials begin to oxidize. From the differences in the slopes, the Ce alloyed sample is initially oxidizing at a faster rate. This increased oxidation rate is beneficial for application of this material in devices, due to the clear correlation between Yb_2O_3 growth and the decrease in sublimation observed by J.A. Nesbitt;[42] therefore, the passivating oxide layer would form faster allowing for decreased sublimation. Thus, prolonging the life of the device. At ~ 900 K, both materials exhibit a slowing oxidation rate, illustrated by the slope becoming more gradual, and they continue to oxidize until 1273 K. A more detailed study of the oxidation resistance of the best performing $Yb_{14}MnSb_{11}$ compounds would be of particular interest for device design.

In Figure 10, $Yb_{13.6}Ce_{0.4}MnSb_{11}$ (1.07 Mn) and $Yb_{14}MnSb_{11}$ are cycled, under flowing Ar, to 1573 K to investigate any improvements to sublimation with these optimized compositions. The $Yb_{13.6}Ce_{0.4}MnSb_{11}$ (1.07 Mn) sample exhibits a small mass loss (~1%) below 573 K most likely from moisture loss of the alumina crucibles. The remaining cycles lose less than 0.1% of the mass signifying that there is no sublimation under the Ar flow. The $Yb_{14}MnSb_{11}$ sample also does not exhibit sublimation upon heating; however, as the temperature increases there is a slight increase in mass of ~0.3%, with a more obvious

increase at ~ 1300 K, that is likely attributed to oxidation from impurities in the ultra-high purity argon. There is no further mass gain or loss in the remaining cycles, illustrating that the $Yb_{14}MnSb_{11}$ sample is not sublimating. This finding is in opposition to what has been previously reported on bulk samples of $Yb_{14}MnSb_{11}$ showing ~0.25% mass loss.[8] The improved quality of $Yb_{14}MnSb_{11}$ prepared by a similar metallurgical route as described herein is likely important for these findings.

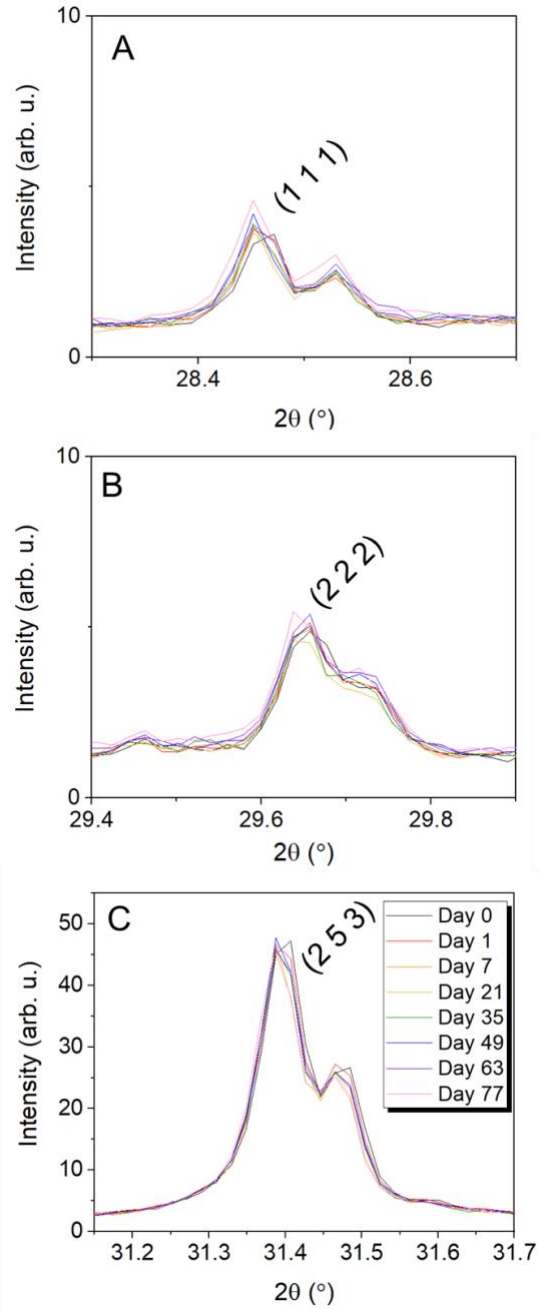

Figure 8: Selected PXRD peaks for the oxidation study of $Yb_{13.6}Ce_{0.4}MnSb_{11}$ (1.07 Mn) after 0, 1, 7, 21, 35, 49, 63, and 77 days in air, where (A) is the Si standard peak (1 1 1), (B) is the Yb_2O_3 peak (2 2 2), and (C) is the (2 5 3) diffraction peak of $Yb_{13.6}Ce_{0.4}MnSb_{11}$ (1.07 Mn). Each image contains both Kα1 and Kα2 from the Cu source.

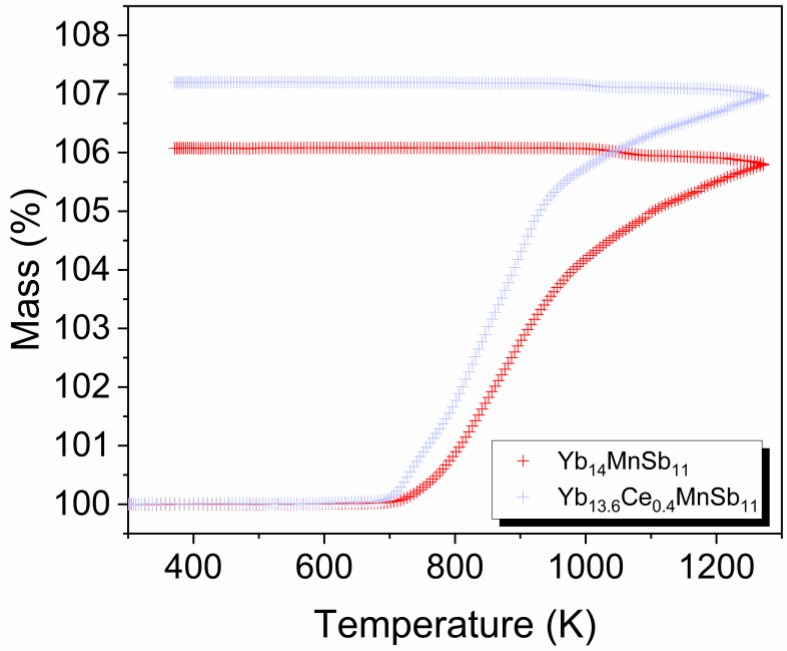

Figure 9: TG under air flow (50 mL/min) of $Yb_{14}MnSb_{11}$ and $Yb_{13.6}Ce_{0.4}MnSb_{11}$ from 300 K to 1273 K (10 K/min).

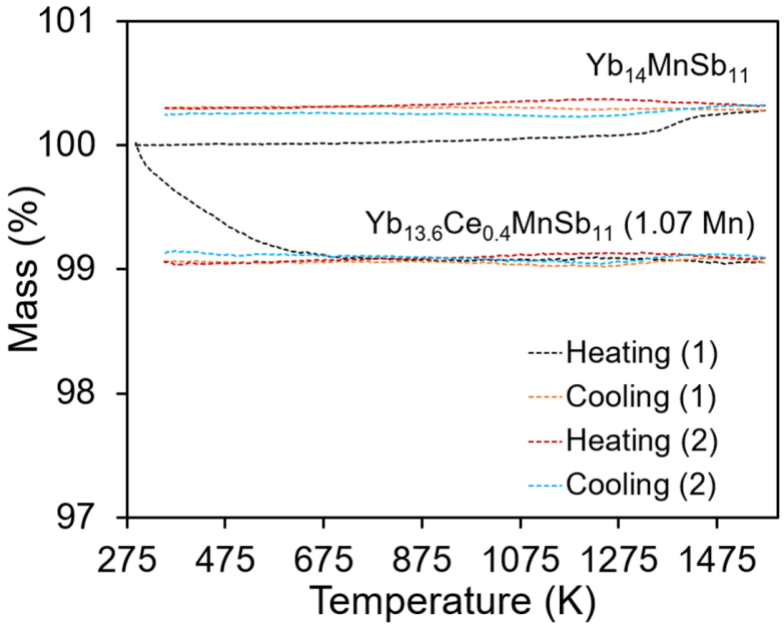

Figure 10: Cycled TG under Ar flow (50 mL/min) of $Yb_{14}MnSb_{11}$ and $Yb_{13.6}Ce_{0.4}MnSb_{11}$ from 300 K to 1573 K (10 K/min).

Conclusions

Samples of $Yb_{13.6}Ce_{0.4}MnSb_{11}$ with different amounts of Mn (z = 1, 1.05, 1.07, 1.1) were prepared. The sample with the best resulting TE properties was prepared with 1.07 Mn and Ce = 0.44; giving rise to a max zT = 1.21 at 1200 K. Ce^{3+} substituted $Yb_{14}MnSb_{11}$ has a reduced carrier concentration compared to $Yb_{14}MnSb_{11}$, as expected from the electron donation from Ce^{3+}. The electron donation contributes to the reduction of the bandgap and induces bipolar conduction at high temperature. Additionally, the increased Seebeck coefficient and reduced thermal conductivity of $Yb_{13.6}Ce_{0.4}MnSb_{11}$ are the main responsible for improving the ZT_{avg} (0.80) when compared to $Yb_{14}MnSb_{11}$ (0.71). The $Yb_{13.6}Ce_{0.4}MnSb_{11}$ (1.07 Mn) sample was exposed to air oxidation for 77 days without any evidence of degradation. $Yb_{14}MnSb_{11}$ and $Yb_{13.6}Ce_{0.4}MnSb_{11}$ are both resistant to oxidation in air until ~700 K and the increased rate of the formation of the oxide layer in the Ce alloyed sample would be beneficial for long term device stability for space exploration. $Yb_{14}MnSb_{11}$ and $Yb_{13.6}Ce_{0.4}MnSb_{11}$ do not sublimate under a flow of Ar when cycled from 300 K – 1573 K. Given the positive impact of Ce substitution, further improvements will focus on the Mn and Sb sites to optimize zT while retaining the benefits of the RE alloying.

Supporting Information

Supporting information contains additional PXRD diffraction data of MnSb precursors, experimental data with fittings, EMPA backscatter images and mapping, Rietveld refinement plots, TE data of higher oxide content samples, Refinement data of higher oxide content samples, and PXRD oxide study of $Yb_{14}MnSb_{11}$.

Acknowledgments

The authors thank Gregory Baxter and Nick Botto for the electron microprobe measurements. Financial support from NEUP and NSF DMR-1709382 is gratefully acknowledged. Part of this research was carried out at the Jet Propulsion Laboratory, California Institute of Technology, under a contract with the National Aeronautics and Space Administration, supported by the NASA Science Mission Directorate's Radioisotope Power Systems. G. Cerretti's research at Jet Propulsion Laboratory was supported by an appointment to the NASA Postdoctoral Program, administered by Universities Space Research Association under contract with NASA.

References

(1) Hu, Y.; Cerretti, G.; Kunz Wille, E. L.; Bux, S. K.; Kauzlarich, S. M. The Remarkable Crystal Chemistry of the $Ca_{14}AlSb_{11}$ Structure Type, Magnetic and Thermoelectric Properties. *J. Solid State Chem.* **2019**, *271* (December 2018), 88–102. https://doi.org/10.1016/j.jssc.2018.12.037.

(2) Kazem, N.; Kauzlarich, S. M. Thermoelectric Properties of Zintl Antimonides. *Handb. Phys. Chem. Rare Earths* **2016**, *50*, 177–208. https://doi.org/10.1016/bs.hpcre.2016.05.003.

(3) Liu, K.-F. F.; Xia, S.-Q. Q. Recent Progresses on Thermoelectric Zintl Phases: Structures, Materials and Optimization. *J. Solid State Chem.* **2019**, *270* (November 2018), 252–264. https://doi.org/10.1016/j.jssc.2018.11.030.

(4) Ovchinnikov, A.; Bobev, S. Zintl Phases with Group 15 Elements and the Transition Metals: A Brief Overview of Pnictides with Diverse and Complex Structures. *J. Solid State Chem.* **2019**, *270* (November 2018), 346–359. https://doi.org/10.1016/j.jssc.2018.11.029.

(5) Beretta, D.; Neophytou, N.; Hodges, J. M.; Kanatzidis, M. G.; Narducci, D.; Martin-

Gonzalez, M.; Beekman, M.; Balke, B.; Cerretti, G.; Tremel, W.; Zevalkink, A.; Hofmann, A.I.; Muller, C.; Dorling, B.; Campoy-Quiles, M.; Caironia, M. Thermoelectrics: From History, a Window to the Future. *Mater. Sci. Eng. R Reports* **2019**, *138* (July 2018), 210–255. https://doi.org/10.1016/j.mser.2018.09.001.

(6) Rock, J. L.; Fleurial, J.-P.; Hendricks, T. Path To A Next Generation RadioIsotope Thermoelectric Generator (RTG). In *Nuclear and Emerging Technologies for Space, Americann Nuclear Society Topical Meeting*; 2019; p 3.

(7) Fleurial, J.-P.; Bux, S. K.; Caillat, T. Engineering of Novel Thermoelectric Materials and Devices for Next Generation, Long Life, 20% Efficient Space Power Systems. In *11th Internation Energy Conversion Engineering Conference. Thermoelectric Devices and Systems: Thermoelectric Devices and Systems.*; 2013.

(8) Grebenkemper, J. H.; Hu, Y.; Barrett, D.; Gogna, P.; Huang, C.-K. C. K.; Bux, S. K.; Kauzlarich, S. M. High Temperature Thermoelectric Properties of $Yb_{14}MnSb_{11}$ Prepared from Reaction of MnSb with the Elements. *Chem. Mater.* **2015**, *27* (16), 5791–5798. https://doi.org/10.1021/acs.chemmater.5b02446.

(9) Peng, W.; Chanakian, S.; Zevalkink, A. Crystal Chemistry and Thermoelectric Transport of Layered AM_2X_2 Compounds. *Inorg. Chem. Front.* **2018**, *5* (8), 1744–1759. https://doi.org/10.1039/c7qi00813a.

(10) Brown, S. R.; Kauzlarich, S. M.; Gascoin, F.; Snyder, G. J.; Jeffrey Snyder, G. $Yb_{14}MnSb_{11}$: New High Efficiency Thermoelectric Material for Power Generation. *Chem. Mater.* **2006**, *18* (7), 1873–1877. https://doi.org/10.1021/cm060261t.

(11) Kim, H. S.; Liu, W.; Chen, G.; Chu, C. W.; Ren, Z. Relationship between Thermoelectric Figure of Merit and Energy Conversion Efficiency. *Proc. Natl. Acad. Sci. U. S. A.* **2015**, *112* (27), 8205–8210. https://doi.org/10.1073/pnas.1510231112.

(12) Kim, H. S.; Liu, W.; Ren, Z. The Bridge between the Materials and Devices of Thermoelectric Power Generators. *Energy Environ. Sci.* **2017**, *10* (1), 69–85. https://doi.org/10.1039/c6ee02488b.

(13) Cheikh, D.; Hogan, B. E.; Vo, T.; Von Allmen, P.; Lee, K.; Smiadak, D. M.; Zevalkink, A.; Dunn, B. S.; Fleurial, J. P.; Bux, S. K. Praseodymium Telluride: A High-Temperature, High-ZT Thermoelectric Material. *Joule* **2018**, *2* (4), 698–709. https://doi.org/10.1016/j.joule.2018.01.013.

(14) Cordier, G.; Schäfer, H.; Stelter, M.; Schafer, H.; Stelter, M. Darstellung Und Struktur Der Verbindung $Ca_{14}AlSb_{11}$. *ZAAC - J. Inorg. Gen. Chem.* **1984**, *519* (12), 183–188. https://doi.org/10.1002/zaac.19845191219.

(15) Chan, J. Y.; Olmstead, M. M.; Kauzlarich, S. M.; Webb, D. J.; Kauzlarih, S. M.; Webb, D. J. Structure and Ferro Magnetism of the Rare-Earth Zintl Compounds: $Yb_{14}MnSb_{11}$ and $Yb_{14}MnBi_{11}$. *Chem. Mater.* **1998**, *10* (11), 3583–3588. https://doi.org/10.1021/cm980358i.

(16) Holm, A. P.; Kauzlarich, S. M.; S.A., M.; Waddill, G. D.; Pickett, W. E.; Tobin, J. G.; Morton, S. A.; Waddill, G. D.; Pickett, W. E.; Tobin, J. G. XMCD Characterization of the Ferromagnetic State of $Yb_{14}MnSb_{11}$. *J. Am. Chem. Soc.* **2002**, *124* (33), 9894–9898. https://doi.org/10.1021/ja020564y.

(17) Grebenkemper, J. H.; Klemenz, S.; Albert, B.; Bux, S. K.; Kauzlarich, S. M. Effects of Sc and Y Substitution on the Structure and Thermoelectric Properties of $Yb_{14}MnSb_{11}$. *J. Solid State Chem.* **2016**, *242* (242), 55–61. https://doi.org/10.1016/j.jssc.2016.03.015.

(18) Hu, Y. F.; Bux, S. K.; Grebenkemper, J. H.; Kauzlarich, S. M. The Effect of Light Rare Earth Element Substitution in $Yb_{14}MnSb_{11}$ on Thermoelectric Properties. *J. Mater. Chem. C* **2015**, *3* (40), 10566–10573. https://doi.org/10.1039/c5tc02326b.

(19) Toberer, E. S.; Brown, S. R.; Ikeda, T.; Kauzlarich, S. M.; Jeffrey Snyder, G.; Snyder, G. J. High Thermoelectric Efficiency in Lanthanum Doped $Yb_{14}MnSb_{11}$. *Appl. Phys. Lett.* **2008**, *93* (6), 12–15. https://doi.org/10.1063/1.2970089.

(20) Roudebush, J. H.; Grebenkemper, J.; Hu, Y.; Kazem, N.; Abdusalyamova, M. N.; Kauzlarich, S. M. $Yb_{14-x}Tm_xMnSb_{11}$ ($0<x<0.5$): Structure and Magnetic Properties. *J. Solid State Chem.* **2014**, *211*, 206–211. https://doi.org/10.1016/j.jssc.2013.12.023.

(21) Yu, C.; Chen, Y.; Xie, H.; Snyder, G. J.; Fu, C.; Xu, J.; Zhao, X.; Zhu, T. Improved Thermoelectric Properties in Lu-Doped $Yb_{14}MnSb_{11}$ Zintl Compounds. *Appl. Phys. Express* **2012**, *5* (3), 31801. https://doi.org/10.1143/apex.5.031801.

(22) Vasilyeva, I.; Abdusalyamova, M. N.; Makhmudov, F.; Eshov, B.; Kauzlarich, S. M. Thermal Air-Oxidized Coating on $Yb_{14-x}RE_xMnSb_{11}$ Ceramics: The Role of Rare Earth Dopants. *J. Therm. Anal. Calorim.* **2019**, *136* (2), 541–548. https://doi.org/10.1007/s10973-018-7659-z.

(23) Prakash, J.; Stoyko, S.; Voss, L.; Bobev, S. On the Extended Series of Quaternary Zintl Phases $Ca_{13}REMnSb_{11}$ (RE = La–Nd, Sm, Gd–Dy). *Eur. J. Inorg.*

Chem. **2016**, *2016* (18), 2912–2922. https://doi.org/10.1002/ejic.201600306.

(24) Grebenkemper, J. H.; Kauzlarich, S. M. Magnetic and Structural Effects of Partial Ce Substitution in $Yb_{14}MnSb_{11}$. *APL Mater.* **2015**, *3* (4), 41503. https://doi.org/10.1063/1.4908038.

(25) Toby, B. H.; Von Dreele, R. B. GSAS-II: The Genesis of a Modern Open-Source All Purpose Crystallography Software Package. *J. App. Crystal.* **2013**, *46* (2), 544–549.

(26) Ravi, V.; Firdosy, S.; Caillat, T.; Brandon, E.; Van Der Walde, K.; Maricic, L.; Sayir, A. Thermal Expansion Studies of Selected High-Temperature Thermoelectric Materials. *J. Electron. Mater.* **2009**, *38* (7), 1433–1442. https://doi.org/10.1007/s11664-009-0734-2.

(27) Zoltan, D.; Wood, C.; Stapfer, G. Measurement of Seebeck Coefficient Using a Light Pulse. *Proc. Intersoc. Energy Convers. Eng. Conf.* **1984**, *719* (October 1984), 2241–2243.

(28) Borup, K. A.; Toberer, E. S.; Zoltan, L. D.; Nakatsukasa, G.; Errico, M.; Fleurial, J. P.; Iversen, B. B.; Snyder, G. J. Measurement of the Electrical Resistivity and Hall Coefficient at High Temperatures. *Rev. Sci. Instrum.* **2012**, *83* (12). https://doi.org/10.1063/1.4770124.

(29) Kainzbauer, P.; Richter, K. W.; Ipser, H. Experimental Investigation of the Binary Mn-Sb Phase Diagram. *J. Phase Equilibria Diffus.* **2016**, *37* (4), 459–468. https://doi.org/10.1007/s11669-016-0470-2.

(30) Brauer, V. G.; Gradinger, H. Uber Heterotype Mischphasen Bei Seltenerdoxyden. *Zeitschrift fur Anorg. und Allg. Chemie* **1954**, *276* (5–6), 209–348. https://doi.org/10.1002/zaac.200690020.

(31) Mandal, B. P.; Grover, V.; Roy, M.; Tyagi, A. K. X-Ray Diffraction and Raman Spectroscopic Investigation on the Phase Relations in Yb_2O_3- and Tm_2O_3-Substituted CeO_2. *J. Am. Ceram. Soc.* **2007**, *90* (9), 2961–2965. https://doi.org/10.1111/j.1551-2916.2007.01826.x.

(32) Sales, B. C.; Khalifah, P.; Enck, T. P.; Nagler, E. J.; Sykora, R. E.; Jin, R.; Mandrus, D. Kondo Lattice Behavior in the Ordered Dilute Magnetic Semiconductor $Yb_{14-x}La_xMnSb_{11}$. *Phys. Rev. B - Condens. Matter Mater. Phys.* **2005**, *72* (20), 1–5. https://doi.org/10.1103/PhysRevB.72.205207.

(33) Wu, Z.; Li, J.; Li, X.; Zhu, M.; Wu, K. C.; Tao, X. T.; Huang, B. B.; Xia, S. Q. Tuning the Thermoelectric Properties of $Ca_9Zn_{4+x}Sb_9$ by Controlled Doping on the

Interstitial Structure. *Chem. Mater.* **2016**, *28* (19), 6917–6924. https://doi.org/10.1021/acs.chemmater.6b02498.

(34) Brown, S. R.; Kauzlarich, S. M.; Gascoin, F.; Jeffrey Snyder, G. High-Temperature Thermoelectric Studies of $A_{11}Sb_{10}$ (A=Yb, Ca). *J. Solid State Chem.* **2007**, *180* (4), 1414–1420. https://doi.org/http://dx.doi.org/10.1016/j.jssc.2007.02.007.

(35) Wang, H.; Pei, Y.; LaLonde, A. D.; Snyder, G. J. Heavily Doped P-Type PbSe with High Thermoelectric Performance: An Alternative for PbTe. *Adv. Mater.* **2011**, *23* (11), 1366–1370. https://doi.org/10.1002/adma.201004200.

(36) Gibbs, Z. M.; Kim, H.-S.; Wang, H.; Snyder, G. J. Band Gap Estimation from Temperature Dependent Seebeck Measurements from the 2e|S|maxTmax Relation. *Appl. Phys. Lett.* **2015**, *106*, 022112.

(37) Justl, A. P.; Cerretti, G.; Bux, S. K.; Kauzlarich, S. M. Hydride Assisted Synthesis of the High Temperature Thermoelectric Phase: $Yb_{14}MgSb_{11}$. *J. Appl. Phys.* **2019**, *126* (16). https://doi.org/10.1063/1.5117291.

(38) Wille, E. L. K.; Grewal, N. S.; Bux, S. K.; Kauzlarich, S. M. Seebeck and Figure of Merit Enhancement by Rare Earth Doping in $Yb_{14-x}RE_xZnSb_{11}$ (x = 0.5). *Materials (Basel).* **2019**, *12* (5), 1–12. https://doi.org/10.3390/ma12050731.

(39) Uvarov, C. A.; Abdusalyamova, M. N.; Makhmudov, F.; Star, K.; Fleurial, J.-P.; Kauzlarich, S. M. The Effect of Tm Substitution on the Thermoelectric Performance of $Yb_{14}MnSb_{11}$. *Sci. Adv. Mater.* **2011**, *3* (4), 652–658.

(40) Fisher, I. R.; Wiener, T. A. A.; Bud'ko, S. L.; Canfield, P. C. C.; Chan, J. Y.; Kauzlarich, S. M.; Bud'ko, S. L.; Canfield, P. C. C. Thermodynamic and Transport Properties of Single-Crystal $Yb_{14}MnSb_{11}$. *Phys. Rev. B.* **1999**, *59* (21), 13829–13834. https://doi.org/10.1103/PhysRevB.59.13829.

(41) Wang, Y.; Hu, Y. J.; Firdosy, S. A.; Star, K. E.; Fleurial, J. P.; Ravi, V. A.; Chen, L. Q.; Shang, S. L.; Liu, Z. K. First-Principles Calculations of Lattice Dynamics and Thermodynamic Properties for $Yb_{14}MnSb_{11}$. *J. Appl. Phys.* **2018**, *123* (4). https://doi.org/10.1063/1.5013601.

(42) Nesbitt, J. A. Rate of Sublimation of $Yb_{14}MnSb_{11}$, a Thermoelectric Material for Space Power Applications. *J. Electron. Mater.* **2014**, *43* (9), 3128–3137. https://doi.org/10.1007/s11664-014-3261-8.

(43) Holm, A. P.; Ozawa, T. C.; Kauzlarich, S. M.; Morton, S. A.; Waddill, G. D.; Tobin, J. G. X-Ray Photoelectron Spectroscopy Studies of $Yb_{14}MnSb_{11}$ and $Yb_{14}ZnSb_{11}$.

J. Solid State Chem. **2005**, *178* (1), 262–269.
https://doi.org/10.1016/j.jssc.2004.07.009.